Aerosol and Air Quality Research, 15: 2445–2455, 2015

ISSN: 1680-8584 print / 2071-1409 online
doi: 10.4209/aaqr.2015.04.0280

Simultaneous Removal of Particulate Matter and Gas-Phase Pollutants within Electrostatic Precipitators: Coupled In-Flight and Wall-Bounded Adsorption

Herek L. Clack*

Department of Civil and Environmental Engineering, University of Michigan, 2350 Hayward Street, Ann Arbor, Michigan 48109, USA

ABSTRACT

Older combustion facilities are favored to comply with imposed regulations limiting emissions of trace toxic metals by modifying the operation of existing emissions control devices to concurrently capture the regulated toxic metal compound; a prominent example of this is adsorption of mercury by added activated carbon within electrostatic precipitators (ESPs). Our previous quasi-1-D analyses employed simplifying assumptions, some of which were initially proposed decades ago. The present study leverages a modern computational platform to remove restrictive, simplifying assumptions and capture details of multi-phase flows and electric and electro-hydrodynamic phenomena that were previously out of computational reach. The results reveal the conflicting interdependent trends in particulate matter (PM) collection and adsorption of a trace gas-phase pollutant, assumed here to be mercury. In particular, we show the power of the inverse correlation between PM removal efficiency and trace pollutant adsorption efficiency, for two representative particle size distributions for increasing treatment times and under constant electrical conditions (applied voltage and current density). Also noteworthy is the finding that the two mechanisms of trace pollutant adsorption within an ESP, in-flight adsorption by suspended sorbent particles and wall-bounded adsorption by sorbent-covered walls, cannot be treated as additive. Wall-bounded adsorption depletes trace pollutant concentrations in the concentration boundary layer near the walls, reducing the driving potential for in-flight adsorption in these regions. For the conditions simulated, the additional rate of pollutant removal by the former is almost entirely counter-balanced by diminished rates of pollutant removal by the latter. Such findings highlight the need to optimize emissions control processes originally designed for a single pollutant but operated for the purpose of dual-pollutant control.

Keywords: Coal; Mercury; Activated carbon; Flue gas; Toxic metals.

INTRODUCTION

Despite the successful technology demonstrations and the extensive knowledge base that has developed over more than a decade of full-scale testing of mercury emissions control technologies, there remain some unexplained operational excursions. For the most part, such excursions were either intermittent or sporadic and/or constituted only a minor challenge to operations. However, for full-scale tests of powdered sorbent injection upstream of an existing electrostatic precipitator (ESP), (1) the expectation of high mercury removal efficiency while also maintaining high particulate matter (PM) removal efficiency within a device designed for only the latter of those objectives makes such excursions unsurprising, and (2) the internal inaccessibility of operating ESPs leaves only inlet/outlet process stream measurements available for diagnosing phenomena, increasing the value of understanding any operational excursions. Of eight full-scale tests evaluated previously (Clack, 2012), operational excursions such as increased ESP spark rate or stack opacity were reported for four units during PAC injection. Excursions in ESP electrical parameters during PAC injection operations are not surprising given that particle resistivity is an important parameter in ESP operation and performance, and therefore adding finely ground carbonaceous PAC to flue gas containing mineral fly ash will lead to a mixed aerosol having altered properties, perhaps profoundly in some circumstances. Although it has not been possible so far to interrogate operating ESPs for changes in their PM collection, Clack *et al.* (2013) analyzed carbon and mercury concentrations in ESP hoppers during a PAC injection test and found general increases from front to rear in both, suggesting a fractionation-type process in which fly ash is collected more efficiently than PAC in each field, allowing PAC to remain suspended in the flue gas for a longer period of time, affording greater opportunity

* Corresponding author.
Tel.: 1-734-763-6830; Fax: 734-764-4292
E-mail address: hclack@umich.edu

for in-flight mercury adsorption. Therein lies a potential paradox: poor electrical properties of PAC (and small mean particle size) contributing to lower rates of PAC collection - an advantage for in-flight adsorption of mercury but potentially a disadvantage for the overall PAC removal efficiency in an ESP. In-flight mercury adsorption is greatly favored over wall-bounded adsorption within ESPs on a mass transfer basis (Clack, 2006a, b). However, here too, sporadic cases where full-scale PAC injection testing exhibited operational excursions have the potential to inform our understanding of the details of mercury adsorption within ESPs that lies beyond current diagnostic abilities. Data (ADA-ES, 2003a, b; ADA-ES, 2006; Butz *et al.*, 2006) from continuous mercury monitors indicated much slower responses in ESP outlet mercury concentrations to the termination of PAC injection than to its initiation. Such asymmetric responses in mercury removal efficiency to changes in the upstream dosing of powdered mercury sorbents in the flue gas suggests a hysteresis derived from a mercury removal mechanism not based on the concentrations of suspended aerosols in the flue gas.

Generally, the available project reports for the subset of full-scale PAC injection field tests that are public available have lacked detailed ESP operational data and design specifications. As a result, it is not possible to identify similarities or differences between test site conditions that could be correlated with the occurrence or absence of observed ESP operational excursions. The present analysis represents the latest in a continuing effort to establish a more complete understanding of simultaneous mercury adsorption and PM removal within ESPs, in anticipation of future operational excursions that are likely to occur as U.S. electric utilities deploy PAC injection along with other mercury control technologies in advance of the MATS deadline. In the absence of *in situ* measurements, ESPs operated for combined PM and mercury emissions control remain experimentally inscrutable, leaving numerical simulation, validated by field data where possible, as the most feasible means for both addressing operational excursions of either pollutant and inferring internal details of the process from gross performance measures such as flue gas mercury concentrations (and short-term excursions) at the ESP outlet and mercury concentrations (and distributions) among the collected ash in ESP hoppers. The present analysis uses the operational conditions reported during full-scale PAC injection testing at AmerenUE's Meramec site, along with engineering drawings of the ESP involved, to simulate simultaneous mercury and PM removal and examine how key parameters affect their separate performance metrics differently. Specifically, and in a marked improvement over our previous analyses, the present analysis incorporates the non-uniform electric field and space charge density and their effects on both the fluid flow (as a result of electro-hydrodynamic forces) and the motion of the charged particles (as a result of Coulombic forces). While the present study focuses on mercury as the trace pollutant and PAC as the suspended sorbent particles, other trace gas-phase pollutants (e.g., SO_x, non-mercury metals) and other suspended sorbent particles (e.g., hydrated lime, Trona, fly ash, non-carbon mercury sorbents) could also be considered using the present approach if relevant property data (e.g., gas diffusivities, sorbent reactivity and capacity data, and particle electrical properties) were available.

METHODS

The numerical simulation results represent the solution of the steady conservation equations for the electric field; the fluid flow field including electro-hydrodynamic forces; the charged-induced motion of polydisperse suspended solid particles and the evolution of their concentrations; gas-particle mass transfer rates and gas-phase mercury concentration as particles are removed from the fluid flow upon collision with the collection electrodes. The analysis considers two 2-D computational domains: either a 3-wire 2 m × 0.3 m (L × W) segment or a 9-wire 5 m × 0.3 m segment of a complete ESP channel. The high aspect ratios typical of such channels (greater than 10:1 H × W) favor a 2-D assumption, although more recent discharge electrode designs (e.g., coiled wires) undoubtedly promote 3-D phenomena. The cylindrical wires (1 mm diameter, 0.5 m spacing) represent the wire discharge electrodes positioned along the channel centerline, with the channel walls representing the electrically grounded collection electrodes. Only considering three-wire and nine-wire segments is an acknowledgement of the high computational cost in modeling a complete ESP channel. Such cost is not justified in the absence of electrical, fluid dynamic, particle and/or mercury concentration measurements against which such solutions could be compared.

Electric Field

The electric conservation equations govern the electric potential (voltage) distribution in the section, subject to the applied boundary conditions. The electric field is assumed to depend only on the continuous phase fluid properties, and therefore can be solved independently of the fluid flow. The electric field is related to the electric potential by Eq. (1):

$$-\nabla \Phi = \vec{E} \tag{1}$$

where Φ is voltage [V] and $\vec{E}$ is the electric field vector [V m^{-1}]. The solution to Eq. (1) must also satisfy Eq. (2) (Poisson's equation) and Eq. (3) (current continuity) throughout the domain:

$$\nabla^2 \Phi = -\frac{q_i}{\varepsilon} \tag{2}$$

$$\nabla \bullet \left(\left(b_i \nabla \Phi + \vec{U} \right) q_i + \alpha \nabla q_i \right) = 0 \tag{3}$$

where q_i is the local space charge density [C m^{-3}], ε is the electrical permittivity of the fluid, b_i is the ionic mobility in air (1.6e-4 [m^2 V^{-1} s^{-1}]), α is the ion diffusivity coefficient, and $\vec{U}$ is the fluid velocity vector. Table 1 presents boundary and initial conditions applied for Eqs. (1) through (3). In Eq. (3), for the present analysis, Fickian ion diffusion, $\alpha \nabla q_i$,

Table 1. Boundary conditions, by physical phenomenon.

Physics (module)	Inlet BC	Outlet BC	Collection Electrode BC	Discharge Electrode BC	Properties
Electric Field (.es)	$D = \varepsilon\nabla\Phi = 0$	$D = \varepsilon\nabla\Phi = 0$	$\Phi = 0$	$\Phi = -50$ kV $q_i = \mathrm{A}\ (R/r)^n$	A [C m^{-3}]: 3DE: ~–0.0018 9DE: ~–0.022 n [-] 3DE: ~1.723 9DE: ~1.8
Fluid/Continuous phase (.spf2)	Dry air $T = 180$°C $P = 101.325$ kPa $U_0 = 1.55$ m s^{-1}	Open boundary, $P = 95$ kPa	Solid boundary, no slip	Solid boundary, no slip	
Particle/Dispersed phase (.mm)	Specified particle volume fraction flux ($\phi'' = u\phi$), number density flux ($ND_p'' = uND_p$), and mass loading (0.1 g m^{-3})	Specified particle volume fraction flux ($\phi'' = u\phi$), number density flux ($ND_p'' = uND_p$)	Open boundary	No particle flux, particle bounce	$\rho_p = 0.51$ g cc^{-1} $\varepsilon = 4$ Log-normal distribution ($\overline{d_p} = 20$ µm, $\sigma_g = 1.75$) or skewed distribution, $d_{50} = 17.32$ µm
Transport of dilute species (.chds)	Specified species flux ($N_1'' = u\ C_0$)	Specified species flux ($N_1'' = uC$)	Specified species concentration ($C = 0$)	No species flux ($N_1'' = 0$)	$C_0 = 4 \times 10^{-7}$ mol m^{-3} $MW = 201$ g/gmol $D_{ab} = 3.4 \times 10^{-5}$ m^2 s^{-1}
Transport of dilute species (.chds2)	Specified species flux ($N_2'' = u\ C_0$)	Specified species flux ($N_2'' = uC$)	Specified species flux ($N_2'' = N_1''$)	No species flux ($N_2'' = 0$)	$C_0 = 4 \times 10^{-7}$ mol m^{-3} $MW = 201$ g gmol^{-1} $D_{ab} = 3.4 \times 10^{-5}$ m^2 s^{-1}

is neglected in relation to advection and field-driven ion transport. Further, advection of ions by the fluid, $\vec{U}q_i$ in Eq. (3), is neglected in relation to field-driven ion transport. Zhao and Adamiak (2008) demonstrated that a 3 m s^{-1} gas flow about a wire discharge electrode energized to –29 kV decreased upwind ion propagation by 3–4 cm and increased downwind ion propagation by about 10 cm compared to stagnant fluid conditions. Industrial ESPs are more highly energized (up to –70 kV) and their operators strive for lower superficial gas velocities (1–1.5 m s^{-1}), both of which would diminish the impact on ion propagation of advection by the gas.

The spatial distribution of electric potential within the computational domain can be obtained numerically and independent of the fluid dynamic solution, subject to the specified material properties and applied boundary conditions. The solutions to Eqs. (2) and (3) depend on an appropriately selected space charge density distribution $q_i(x,y)$, one that constrains $\Phi(x,y)$ such that $\nabla q_i(x,y)$ and $\nabla\Phi(x,y)$ satisfy Eqs. (2) and (3). In the present analysis, this is achieved through an external iteration procedure: using the electric potential boundary conditions at the discharge and collection electrodes, an expression for $q_i(x,y)$ is specified, an intermediate solution for $\Phi(x,y)$ obtained, a spatial electric potential solution that can be substituted into Eqs. (2) and (3) to evaluate the congruence of each. Iteration on the initial choice of $q_i(x,y)$ continues until satisfactory congruence is achieved for Eqs. (2) and (3). A higher-level iteration loop is included when seeking to match a specific value of current density, which allows constant-current-density comparisons between simulation results. Graphical examples of these results are reported in a companion publication (Clack, 2016), including validation of this approach using the experimental results for a cylindrical ESP reported by Kallio and Stock (1992). Direct simulation of the corona region nearest the discharge electrode surfaces is beyond the scope of this analysis, however the corona represents only a very small fraction of the domain in which PM and mercury capture is occurring and demonstrated agreement between our simulations and the experimentally measured linear current densities reported by Kallio and Stock (1992) supports a conclusion that detailed simulation of the corona region is not required for accurate simulation of the gross electric field and current flows.

Fluid/Continuous Phase

The electro-hydrodynamically influenced flow is governed by the Reynolds-averaged Navier-Stokes equations (Eqs. (4) and (5)), modified to include an electric body force term ($q_i \nabla\Phi$) associated with the momentum imparted to the fluid by ion flows between the discharge and collection electrodes:

$$\rho\left(\nabla \bullet \vec{U}\right) = 0 \tag{4}$$

$$\rho\left(\vec{U} \bullet \nabla\vec{U}\right) = -\nabla P + \mu\nabla^2\vec{U} + q_i\nabla\Phi \tag{5}$$

In Eqs. (4) and (5) above, $\vec{U}$ is local gas velocity vector [m s^{-1}], P is local pressure [Pa], ρ is gas density [kg m^{-3}], μ is the gas dynamic viscosity [Pa-s], q_i is local space charge density [C m^{-3}], and Φ is local electric potential [V]. The electric body force term in Eq. (5) is dependent on the previously solved distributions of electric potential $\Phi(x,y)$ and associated space charge density $q_i(x,y)$. The fluid is assumed to be incompressible, however the native material property database provides temperature-dependent values of fluid properties. The native k-ε turbulence model is used along with the default turbulence parameters. Table 1 lists the applied initial and boundary conditions during the solution for $\vec{U}$, the distribution of which is used to initialize the fluid flow field for the multi-phase gas-particle mixture.

Particle/Dispersed Phase

Treating the volume fraction and number density of particles within the gas flow as size-dependent scalar variables, their spatial distribution within the ESP channel segment is governed, to first order, by their initial values entering the channel segment and the instantaneous net force exerted on particles in each size class, the integral of which dictates particle trajectories in the channel segment and the rate of particle collisions with and removal from the flow by the channel walls. For particles of the size considered here (< 150 μm) gravitational acceleration can be neglected compared to accelerations due to fluid dynamic drag and Coulombic forces induced by the accumulated particle charge and the imposed electric field. Results are presented for two particle size distributions entering the ESP channel segment, particles representing powdered activated carbon (PAC): a log-normally distributed particle size that is commonly used to represent aerosols, and an algebraic representation of the size distribution measured from an actual powdered activated carbon product, as reported previously (Prabhu *et al.*, 2012). Fig. 1 illustrates the two size distributions considered and Table 1 lists the boundary conditions for the dispersed phase. The two continuous size distributions are approximated by size binning; 11 size bins ($1.5 < d_p < 125$ μm, see Table 1) for the log-normal distribution and 10 size bins ($1.5 < d_p < 85$ μm) for the measured size distribution of the FGD powdered activated carbon product. Solutions for the size-dependent spatial distributions of particle number density $ND_p(x,y,d_p)$ and particle volume fraction $\phi(x,y,d_p)$ for all size bins are computed simultaneously in order to accurately render their collective effect on local gas-phase pollutant concentration $C(x,y)$, assumed here to be mercury. Although mineral fly ash is also present, under most circumstances mercury adsorbed by PAC exceeds that adsorbed by fly ash by a wide margin: Cold-side ESPs averaged 27% baseline mercury removal efficiency and hot-side ESPs averaged 4% (EPRI-reported summary of U.S. EPA Information Collection Request (ICR) data (Chu *et al.*, 2000), as presented in review by Pavlish *et al.* (2003)), justifying a PAC-only analysis. Particle-particle interactions and two-way particle-fluid coupling are beyond the scope of this analysis.

The gas-particle mass transfer rate for particles of size d_p depends on their relative velocity with respect to the gas, or slip velocity $\vec{U}_{slip}$. Outside of the present context, uncharged

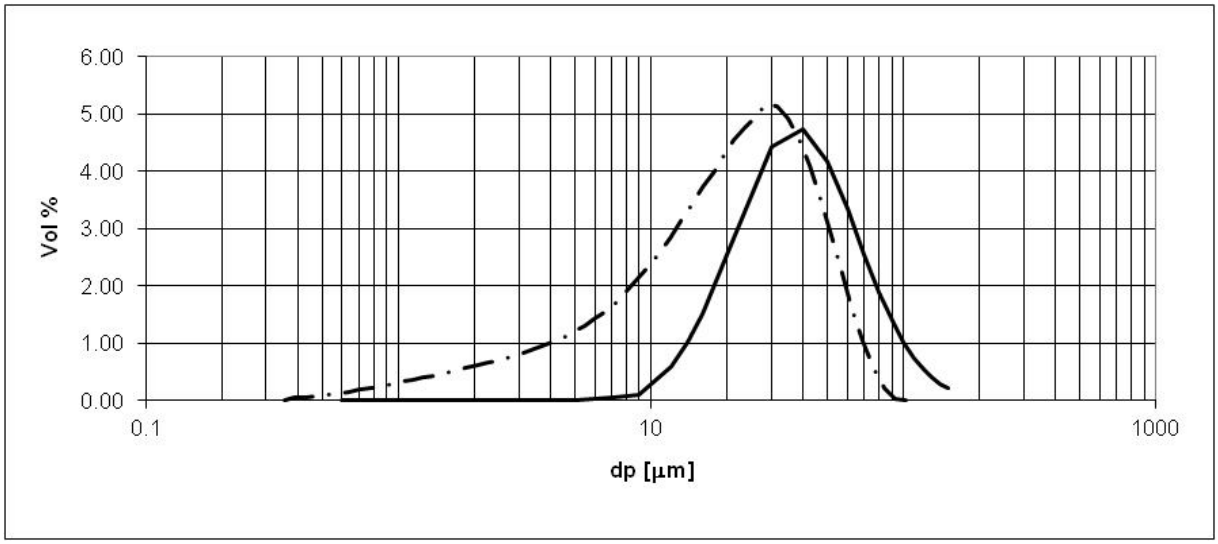

Fig. 1. Particle size distributions assumed in present analysis. Solid line: Log-normal particle size distribution, $\overline{d_p}$ = 20 µm, σ_g = 1.75. Dashed line: Measured size distribution (Prabhu *et al.*, 2012) of FGD powdered activated carbon product, d_{50} = 17.32 µm.

particles typically exhibit $\vec{U}_{slip}$ governed by gravitational acceleration, particle inertia, fluid viscosity, and fluid velocity gradients. For charged particles, electrostatic forces can be an important contributor to $\vec{U}_{slip}$ and gas-particle mass transfer; in addition to particle charging, particularly strong electric fields and electrical discharges can induce electro-hydrodynamic forces on the fluid producing highly articulated fluid flow patterns characterized by local maxima of $\nabla \bullet \vec{U}$ in the fluid and $\vec{U}_{slip}$ for the entrained particles. Thus, in considering in-flight adsorption of mercury within ESPs, gas-particle mass transfer is driven by size-dependent $\vec{U}_{slip}$, which through viscous and electrostatic forces, is also a function of spatially distributed $\Phi(x,y)$ and $q_i(x,y)$. This represents a significant departure from the simplifying assumptions of size-dependent but spatially uniform particle electrostatic drift velocities inherent in analytical ESP performance models such as the Deutsch-Anderson equation, which we have used previously (Clack, 2006a, b; Clack, 2009).

Size-binned representations of the two particle size distributions in Fig. 1 are applied as ESP segment inlet conditions for the dispersed phase in separate analyses that follow, with inlet concentrations in both cases equaling 0.1 g m^{-3}, the equivalent of 6 lbs/MMacf (pounds of PAC per million actual cubic feet of flue gas), corresponding to high rates of PAC usage based on the most recent demonstrations of mercury removal by PAC injection, the effects of PAC on PM collection, and costs. To facilitate numerical convergence, the fluid velocity field derived from the solution of Eqs. (4) and (5) is used to initialize $\vec{U}(x,y)$ of the continuous phase during the solution of the size-dependent, spatial distributions of particle volume fraction $\phi(x,y,d_p)$ and particle number density $ND_p(x,y,d_p)$ of the gas-particle mixture as it flows within the ESP segment. Trajectories of particles of size d_p are governed by the x- and y-components of $\vec{U}_{slip}$, u_{slip} and v_{slip} representing the balance between viscous and Coulombic forces on the particles:

$$u_{slip} = \frac{N_e(-e)E_x C_c}{3\pi\mu d_p} \tag{6}$$

$$v_{slip} = \frac{N_e(-e)E_y C_c}{3\pi\mu d_p} \tag{7}$$

where N_e is the number of elementary charges on each particle, e is the elementary charge of an electron (1.6E-19 C), E_x and E_y are the x- and y-components of the electric field vector $\vec{E}$, and μ and d_p are as previously defined. C_c is the Cunningham slip correction factor:

$$C_c = 1 + Kn\left[1.257 + 0.4\left(\exp\left(\frac{-1.1}{Kn}\right)\right)\right] \tag{8}$$

where Kn, Knudsen number, is defined as λ/d_p and where λ is the gas mean free path evaluated identically as our previous analyses (Clack, 2006b).

Particle charge accumulation is a function of the local electric field $\vec{E}$ and local space charge density $q_i(x,y)$. Transient particle charging near an ESP inlet represents a small fraction of the hydrodynamic or aerosol timescales under typical ESP electrical conditions. A transient particle charging analysis following the method presented in Hinds (1999) and assuming constant values of ρ_i and $\vec{E}$ equal to their average values within these ESP channel segments (1e-5 C m^{-3} and 137,000 V m^{-1}, respectively) shows that after 1 second particles acquire 76% of their saturation charge in the 3-wire segment and 95% of their saturation

charge in the 9-wire segment. For full-scale ESPs operating at similar, representative electrical conditions (–50 kV, 0.11 mA m^{-2}) and whose full-length channels contain dozens of discharge electrodes, the transient charging period would constitute an even smaller fraction of the hydraulic and aerosol timescales, diminishing the error in assuming a constant particle charge equal to its saturation charge. A Lagrangian approach that tracks the ~10^9 particles as they traverse $\vec{E}$ and $q_i(x,y)$ in the channel would be necessary to explicitly calculate the trajectory-dependent transient particle charging period, the importance of which diminishes as channel length increases and channel inlet transient behavior constitutes a diminishing fraction of particle lifetimes in suspension. For these reasons, the present analysis assigns a size-dependent saturation charge to the particles based on the mean values of computed $\vec{E}$ and $q_i(x,y)$ within each ESP segment. Because only super-micron size bins are considered in the present analysis, Eq. (9) represents the number of elementary charges on each particle (N_e), reasonably assumed to be based solely on field charging (Friedlander, 2000):

$$N_e = \left[1 + 2\frac{\varepsilon - 1}{\varepsilon + 2}\right]\frac{Ed_p^2}{4e} \tag{9}$$

where $E = \left|\vec{E}(x,y)\right|$, ε is the particle relative permittivity (dielectric constant) [-], approximated as that of graphite for PAC; and d_p and e are as defined previously. The spatial distribution of particle volume fraction $\phi(x,y,d_p)$ and number density $ND_p(x,y,d_p)$ is governed by the bulk transport of the particles by the continuous phase velocity field $\vec{U}(x,y)$ and the size-dependent slip velocity of particles relative to the continuous phase, $\vec{U}_{slip}$.

For a spherical particle, Eq. (10) (Frössling equation) provides a correlation for evaluating the Sherwood number, a non-dimensional mass transfer parameter the definition of which can be used to solve for the mean convective mass transfer coefficient between a flowing fluid and a sphere ($\overline{h_m}$):

$$\overline{Sh_d} \equiv \frac{\overline{h_m} d_p}{D_{ab}} = 2 + 0.552\left(\frac{\rho\left|\vec{U}_{slip}\right| d_p}{\mu}\right)^{1/2}\left(\frac{\mu}{\rho D_{ab}}\right)^{1/3} \tag{10}$$

where D_{ab} is the binary mass diffusivity of a species in a dilute mixture, here assumed to be elemental mercury diffusing in air (3.4E-5 m^2 s^{-1}, taken from (Clack, 2006b)) and μ, ρ, and d_p are as defined previously. The spatial distribution of the collective rate of gas-particle mass transfer for all particles is subsequently used to calculate the distribution of mercury concentration.

Adsorption of Trace Mercury

The spatial distribution of mercury concentration $C(x,y)$ [mol m^{-3}] is governed by the collective gas-particle mass transfer of adsorbing PAC particles suspended in the fluid flow (in-flight mechanism) and the mass transfer to the layer of collected particles on the ESP segment walls (wall-bounded mechanism). The mass transfer rate between the gas and the surface of each particle associated with mercury adsorption ($\dot{M}_{Hg}$) is given by:

$$\dot{M}_{Hg} = 4\pi\left(\frac{d_p}{2}\right)^2 \overline{h_m} MW\left(C - C_s\right) \tag{11}$$

where C and C_s are the mercury concentrations locally in the gas and at the surface, respectively; all other quantities are as defined previously. For the in-flight mechanism, the reactivity of present-day halogenated powdered sorbents is high enough and typical particle collection times in ESP channels are short enough and that the mercury concentration at the particle surface is assumed to be zero, which along with the local gas-phase mercury concentration ($C(x,y)$) forms the mass transfer potential for gas-particle mass transfer. For the wall-bounded mechanism, concentration boundary layers are calculated along with velocity boundary layers (including electric body forces), along the walls of the ESP channel segments in response to one of the imposed species boundary conditions, shown in Table 1. Mercury removal efficiency in all cases is the percentage difference between inlet species flux and outlet species flux for each channel segment.

COMSOL Multiphysics™ has been previously demonstrated to be suitable for simulating gas-particle phenomena within ESPs (Back and Cramsky, 2012; Clack, 2013) and here version 4.4 served as the platform for coupling and solving the systems of partial differential equations governing the electric field and space charge density (AC/DC module), establishing the baseline flowfield of the coupled electric and fluid dynamic equations (turbulent, single-phase fluid module) that subsequently serves as an initial condition for simultaneously solving for the spatial distribution of charged particle volume fraction and particle slip velocity for the 11 particle sizes into which the two particle size distributions were discretized (mixture module). Using the charged particle volume fraction distributions and slip velocities, gas-particle mass transfer rates are calculated to yield spatial distributions of mercury concentration (trace species chemical transport module); when imposing other than a perfect sink boundary condition for trace chemical transport, a first module with a homogeneous boundary condition (C_s = 0) is employed, following by a second module whose specified species flux boundary condition (N'' = constant) is equated to any desired fraction of that calculated in the first chemical transport module. Using this schema, complete computational times on a 64-bit HP Xeon workstation (2 2.93 GHz processors, 6 Gb RAM) were typically ~60 minutes for the 3-wire in-flight mechanism only, increasing to ~225 minutes for the 3-wire coupled in-flight and wall-bounded mechanisms (13,340 computational elements).

RESULTS AND DISCUSSION

Wall-bounded mercury adsorption by PAC deposited on

ESP channel walls represented a small fraction of the total mercury removal. Velocity and concentration boundary layer development are largely unaffected by the electric body force for EHD flows such as these, dominated instead by the conventional hydrodynamic fluid momentum. This is confirmed when considering the recommended (IEEE-DEIS-EHD Technical Committee, 2003) criteria for onset of significant EHD effects, $N_{EHD} > Re_L^2$ or $Md > Re_L^2$, where:

$$N_{EHD} = \left(\frac{I_0 L^3}{\rho \nu^2 b_i A} \right)^{1/2} \tag{12}$$

$$Md = \frac{\varepsilon_0 E_0^2 L^2}{\rho \nu^2} \tag{13}$$

and $Re_L^2 = U_0^2 L^2 / \nu^2$. I_0 and E_0 are reference values for current and electric field, respectively; L and A are the characteristic length and surface area, respectively, associated with I_0 and E_0; ε_0 is the permittivity of free space (8.85419 $\times 10^{-12}$ [F m^{-1}]), $\nu = \mu/\rho$ [m^2 s^{-1}], and μ, ρ, and b_i are as defined previously. For the significant flow of charge that stable coronas create, the dielectric electric Rayleigh number (Eq. (13)) is not relevant. Based on the N_{EHD} criterion, both the 3-wire and 9-wire ESP channel segments are characterized by values (N_{EHD} = 25.7) that do not exceed Re_L^2 based on the discharge electrode diameter (Re_L^2 = 9260), indicating no significant EHD phenomena are expected, in qualitative agreement with the numerical results.

Considering only the wall-bounded mechanism of mercury removal, removal efficiencies in the ESP channel segments were low. Assuming the most optimistic condition of PAC completely coating the walls, idealized here by treating the walls as perfect adsorbers, 4.7% of the mercury entering the 2 m-long, 3-wire ESP segment was removed, increasing to 7.5% removed in the 5 m-long, 9-wire segment. Such values are lower than those determined previously (Clack, 2006a) based on simplifying assumptions such as uniform electric field, $Re^n Pr^m$ Nusselt number correlations, heat/mass transfer analogy assumptions, and no fluid-electric coupling. The resulting wall-bounded removal efficiencies from those previous analyses for a 50% lower Reynolds number were determined to be less than 10% for a 2-m ESP channel segment and less than 20% for a 5-m ESP channel segment. In an actual ESP, such performance would likely be much lower due to dilution of the wall-deposited PAC by much larger amounts of fly ash, as we have argued previously (Clack, 2006a). Assuming PAC constitutes 2.5% of the PM entering an ESP and deposited on the ESP collection electrodes, a proportional composition for the deposited PM would have the effect of an adsorbing area that was 40 times smaller than the collection electrodes, or equivalently, a 40 times reduction in local mass transfer rate compared to the previous perfect-adsorber boundary condition. Applying this restricted boundary condition yields mercury removal efficiencies of only 0.11% and 0.19% for the 3-wire (2 m) and 9-wire (5 m) channel segments, respectively, values that represent negligible contributions to the overall mercury removal efficiency. Although these simulated ESP channel segments represent only a portion of most utility ESPs, fundamental boundary layer theory holds that mass transfer rate per unit surface area of a flat plate decreases with distance from the leading edge, suggesting that the contribution of the wall-bounded mechanism is not likely to become more prominent at full scale. This is also evident when comparing the results for the two segment lengths: increasing by 2.5 times the ESP channel segment length only yields 1.6 to 1.7 times greater mercury removal. Other factors worthy of consideration include the collected PM in the rearward fields of an ESP becoming enriched in PAC due to slower collection (and greater likelihood of reentrainment) relative to fly ash and an overall decreasing driving potential for boundary layer mass transfer as mercury concentrations in the bulk flue gas decrease. It is also likely that ESP operating conditions leading to significant EHD effects (N_{EHD} or $Md > Re^2$) could produce dramatically altered flowfields, rates of boundary layer growth, and surface species flux.

Considering the in-flight mechanism of mercury removal, Fig. 2 presents numerical results illustrating the streamwise evolution of mercury and total PM concentrations within a 9-wire ESP channel segment. By volume or mass, the vast majority of PM collection occurs early in the channel due to the higher drift velocities of the larger particles and their disproportionate contribution to total mass and total volume.

The competing processes of electrostatic collection of suspended PAC aerosols and in-flight adsorption of mercury by PAC aerosols raises the question of how sensitive is the performance of the latter to the performance of the former. Fig. 3 presents simulation results for mercury, total PM, and $PM_{2.5}$ removal efficiencies for the two ESP channel segments for both the hypothetical log-normal and the actual FGD PAC particle size distributions. Compared to the log-normal size distribution, mercury removal efficiency for the skewed distribution of the FGD PAC is both greater in absolute terms and more sensitive to ESP channel segment length. For a 2.5 times increase in channel segment length, mercury removal efficiency for the log-normal size distribution only increased from 8.3% to 9.5%, compared to a 20 percentage point increase, from 22.9% to 42.6%, for the skewed FGD size distribution. Conversely, total PM and $PM_{2.5}$ removal efficiencies are much lower and less sensitive to channel segment length for the skewed FGD PAC size distribution as compared to the log-normal distribution. These trends are consistent with the skewed FGD PAC size distribution having a greater fraction of its mass held by the smaller particles which collectively present higher surface area (higher mercury removal) and slower charge-driven removal from the gas stream (lower PM removal). Because ESPs can be tasked with removing both PM and trace pollutants, comparisons of the two removal efficiencies may be instructive. Defining the performance ratio, H_R, as the ratio of the primary ESP performance metric (total PM removal efficiency) to the secondary ESP performance metric (in the present case, mercury removal efficiency), for the log-normal size distribution H_R increases approximately proportionally with channel length: increasing channel length by 2.5 times

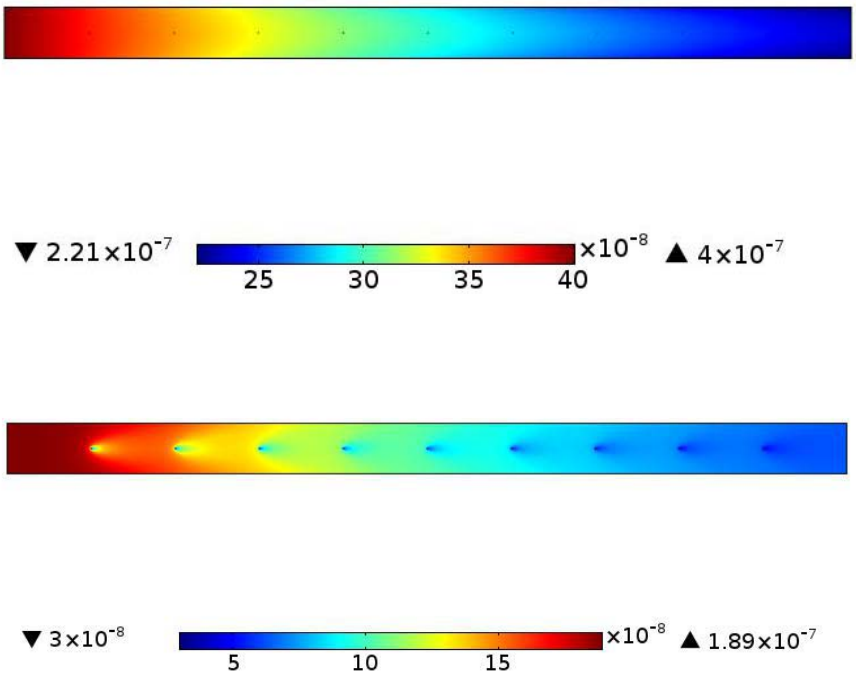

Fig. 2. Results of numerical simulation showing (upper) trace pollutant concentration [mol m^{-3}] and (lower) total PM volume fraction [-] distributions in 9-wire (5 m) ESP channel segment. Conditions as defined in Table 1.

increases H_R by 2.7 times (i.e., H_R(3DE) = 3.735, H_R(9DE) = 10.08). If instead of total PM H_R is based on $PM_{2.5}$ removal efficiency ($H_{R2.5}$), for the log-normal size distribution $H_{R2.5}$ is less than unity for the 3-wire channel and increases by almost a factor of 10 for a 2.5 times increase in channel length (i.e., $H_{R2.5}$(3DE) = 0.217, $H_{R2.5}$(9DE) = 2.16). For the skewed FGD PAC distribution, $H_{R2.5}$(3DE) = 0.06 and $H_{R2.5}$(9DE) = 0.22 which when compared against the log-normal size distribution results strongly shows the impact of the greater abundance of fine particles in the skewed FGD PAC distribution in lowering the $PM_{2.5}$ removal efficiency and increasing the in-flight mercury adsorption. Because H_R and $H_{R2.5}$ will vary with PAC properties and ESP operating conditions, these findings are not fundamental but rather illustrative of how the two competitive and simultaneous processes occurring within ESPs might be parameterized for the purpose of optimizing both, by choice of PAC properties or modification of the ESP control algorithm or physical upgrades to the ESP itself.

Perhaps most interesting are the numerical simulation results combining both the in-flight and wall-bounded mechanisms. In the debate over their relative importance, it has been implicitly assumed that the two mechanisms could be considered independently and when considered together, their effects would be additive. This assumption, however, overlooks their interdependency. Mercury removal through the wall-bounded mechanism produces a growing, mercury-lean concentration boundary layer along the collection electrode through which all charged particles must pass prior to their collection. Furthermore, particle electrostatic drift velocities are likely to be near their minimum values in the relatively weak electric fields adjacent to the collection electrode surface and within the mercury-lean concentration boundary layers. The net effect is prolonged particle presence in a region where in-flight mercury removal is suppressed. When considering both mechanisms together, mercury adsorption at the wall is more than completely offset by the suppression of the in-flight mercury adsorption mechanism within the mercury-lean concentration boundary layer. Fig. 4 compares total in-flight mass transfer rates considering only the in-flight mechanism (Fig. 4, upper) to the coupled in-flight and wall-bounded mechanisms (Fig. 4, lower) for the 3-wire channel segment. In presenting the total in-flight mass transfer rate, Fig. 4 makes clear the reduced values (i.e., less-negative rates of particle-to-gas mass transfer) that are apparent along the walls.

Fig. 5 shows the streamwise evolution of mercury removal efficiency within the 3-wire segment, comparing the in-flight mechanism alone (dashed blue) against the coupled in-flight and wall-bounded mechanisms (dashed red) for the log-normal size distribution. The gradual divergence of the two dashed traces with distance from the channel entrance supports the conceptualization of a primary in-flight adsorption mechanism and a secondary wall-bounded mechanism, the coupling of which gradually degrades their combined performance. Assuming 2.5% of the PM deposited on the collection electrode is PAC, the in-flight mechanism alone achieved higher mercury removal efficiency (8.3%) than the coupled in-flight and wall-bounded mechanisms (8.1%). Similar trends are evident in the results from simulating

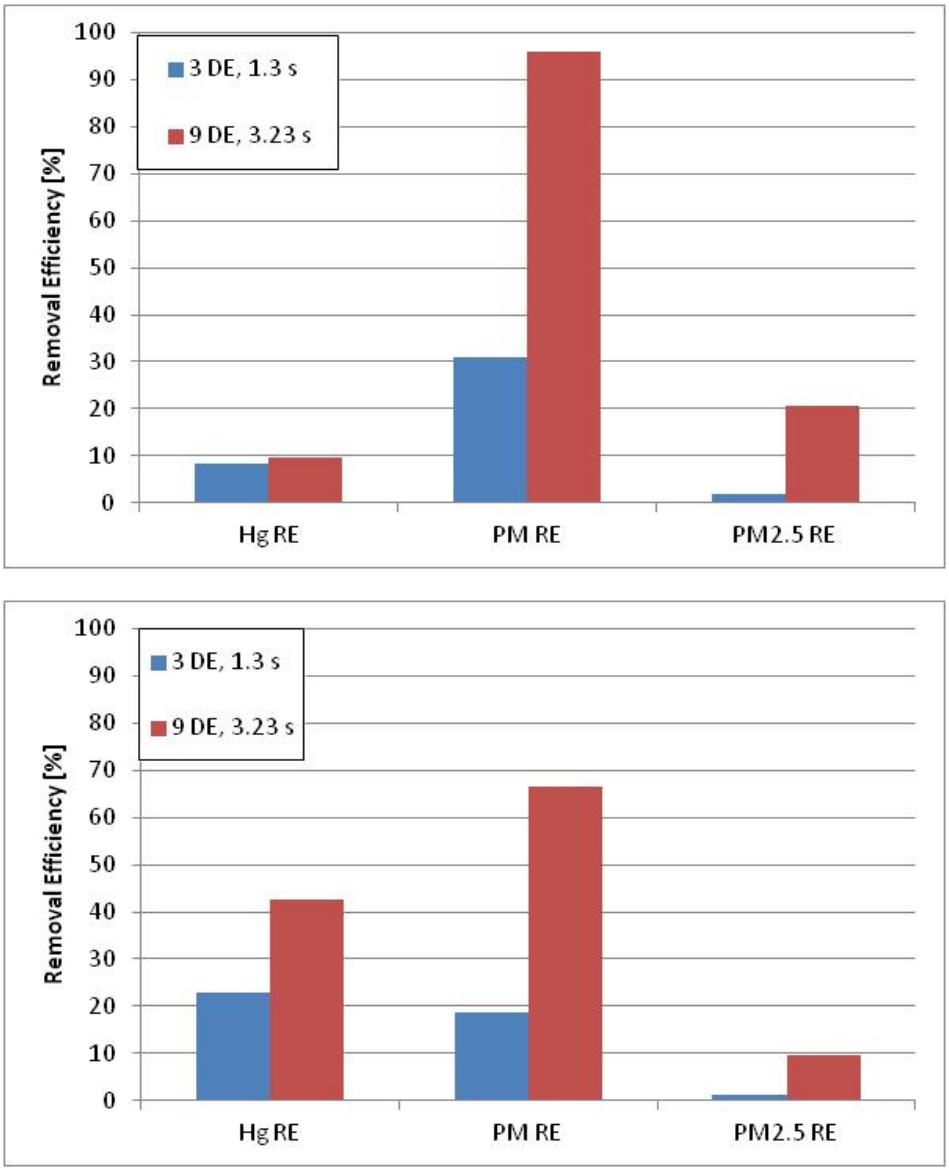

Fig. 3. Removal efficiencies for trace gas-phase pollutant, total PM, and $PM_{2.5}$ during simultaneous electrostatic precipitation and in-flight trace gas adsorption within 3-wire (2 m, 1.3 s) and 9-wire (5 m, 3.23 s) ESP channel segments with constant current density (0.11 mA m^{-2}). Upper: Results for log-normal particle size distribution (d_p = 20 μm, σ_g = 1.75). Lower: Results for skewed FGD PAC particle size distribution (d_{50} = 17.34 μm). All other properties as defined in Table 1.

both mechanisms within the 9-wire segment: higher mercury removal efficiency considering the in-flight mechanism alone (9.5%) compared to the coupled in-flight and wall-bounded mechanisms together (9.2%). This effect is further highlighted in Fig. 5 by plotting the ratio of the coupled mechanism removal efficiency to the in-flight mechanism removal efficiency (solid black). From this ratio it is evident that the two mechanisms initially combine for positive net effect near the entrance to the channel (coupled-to-in-flight removal efficiency ratio greater than unity) but with increasing distance downstream their combined performance becomes less than that of the in-flight mechanism alone (removal efficiency ratio less than unity), appearing to follow a power law dependency with downstream distance (exponent n = –0.016). If the most optimistic wall boundary condition is assumed (100% PAC-covered) for the 9-wire channel segment and the log-normal size distribution, both mechanisms together yield mercury removal efficiency of 16.2%, slightly less than the sum of their separate contributions of 9.5% and 7.5%. These results lend further credibility to the assertion that the in-flight mechanism is the primary source of overall mercury adsorption within ESPs. As noted at the outset, the virtual inability to interrogate the fluid-particle flows within a full-scale ESP leaves no options for validating these numerical simulations of ESP segments using field data. Extending the present numerical approach to simulate a full-scale ESP would require substantially greater computational resources, but would ultimately allow validation of full-scale ESP simulation results against full-scale field data.

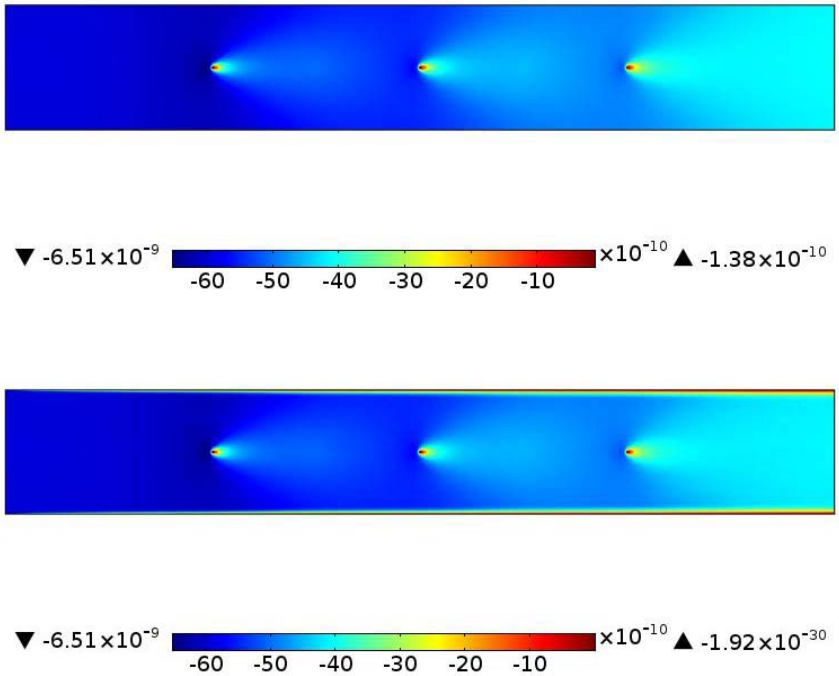

Fig. 4. Total particle-to-gas mass transfer rates for the log-normal particle size distribution in a 3-wire channel segment when (upper) only the in-flight mechanism is considered and (lower) both in-flight and wall-bounded mechanisms for trace pollutant removal are considered. Conditions as defined in Table 1.

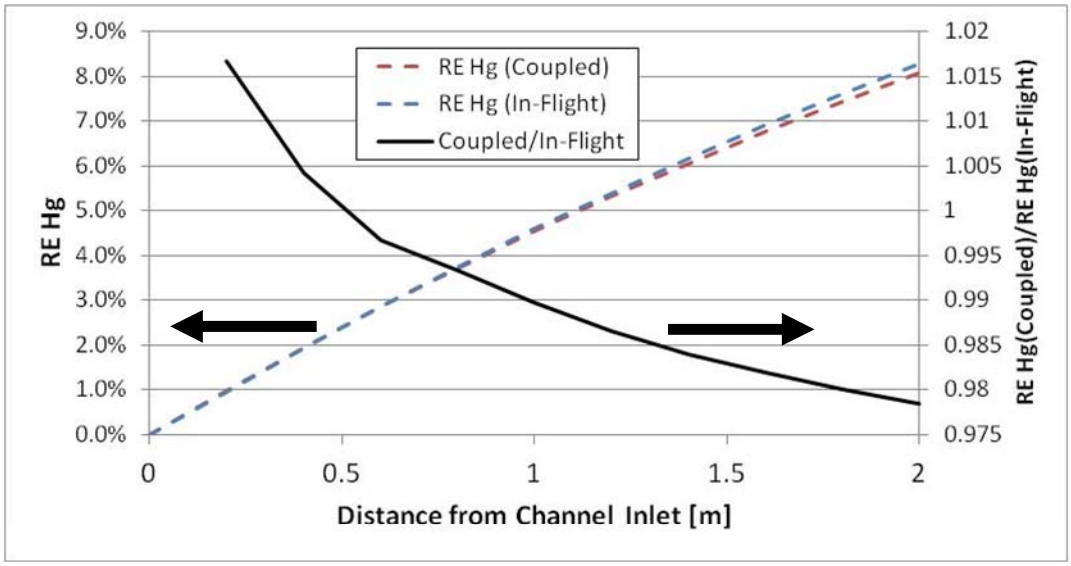

Fig. 5. Streamwise evolution of mercury removal efficiency for in-flight mechanism only (dashed blue), coupled in-flight and wall-bounded mechanisms (dashed red), and ratio of coupled mechanism to in-flight mechanism (solid black). Log-normal size distribution in 3-wire ESP channel assuming 2.5% PAC concentration in collection electrode dustcake. Other conditions as defined in Table 1.

CONCLUSIONS

This study advances understanding of combined particulate removal and trace pollutant removal within industrial electrostatic precipitators, beyond previous study results derived from simplifying, quasi-1-D analyses. Using two different particle size distributions and 2-D simulations of the electric field and space charge density, fluid flow including electric body force, transport of charged particle suspensions, and the gas-particle and fluid-surface mass

transfer processes, the present study finds that wall-bounded mechanisms of trace pollutant removal, assumed in the present study to be mercury removal, are generally quite small compared to the in-flight mechanism of mercury removal. For simultaneous removal of particulate matter and mercury, there is significant sensitivity to properties of the particulate matter; an introduced performance ratio comparing the two pollutants' removal efficiencies reveals the superior particulate removal efficiency for coarser particles versus the superior mercury removal efficiency for finer particles, which in both cases evolves with increasing characteristic hydrodynamic time scales, i.e., with increasing ESP size, as current density is held constant. When considering wall-bounded and in-flight mechanisms of mercury removal within an ESP, it has been shown that the two mechanisms are not additive; the mercury-lean concentration boundary layers that develop along the collection electrodes suppress mass transfer potential for the in-flight mechanism of all particles as they transit the boundary layers prior to collection. The net effect of the additional mercury removed by wall-bounded mechanisms is in most cases almost entirely offset by the reduction in mercury removal by suspended particles and the in-flight mechanism. For all but the most optimistic cases, the combined removal efficiency can be approximated by solely that achieved via the in-flight mechanism.

REFERENCES

ADA-ES (2003a). Final Site Report for: E.C. Gaston Unit 3 - Sorbent Injection into COHPAC for Mercury Control. Field Test Program to Develop Comprehensive Design, Operating, and Cost Data for Mercury Control Systems.

ADA-ES (2003b). Pleasant Prairie Power Plant Unit 2 - Sorbent Injection into a Cold-side ESP for Mercury Control. Final Report, U.S. Department of Energy.

ADA-ES (2006). Evaluation of Sorbent Injection for Mercury Control: Topical Report for DTE Energy's Monroe Station, U.S. Department of Energy, National Energy Technology Laboratory.

Back, A. and Cramsky, J. (2012). Comparison of Numerical and Experimental Results for the Duct-Type Electrostatic Precipitator. *Int. J. Plasma Eng. Sci. Technol.* 6: 33–42.

Butz, J.R., Broderick, T.E. and Turchi, C.S. (2006). Amended Silicates™ for Mercury Control: Project Final Report, National Energy Technology Laboratory, U.S. Dept. of Energy.

Chu, P., Goodman, N., Behrens, C. and Roberson, R. (2000). Total and Speciated Mercury Emissions from U.S. Coal-fired Power Plants, McLean, VA.

Clack, H.L. (2006a). Mass Transfer within Electrostatic Precipitators: Trace Gas Adsorption by Sorbent-covered Plate Electrodes. *J. Air Waste Manage. Assoc.* 56: 759–766.

Clack, H.L. (2006b). Mass Transfer within ESPs: In-flight Adsorption of Mercury by Charged Suspended Particulates. *Environ. Sci. Technol.* 40: 3617–3622.

Clack, H.L. (2006c). Particle Size Distribution Effects on Gas-Particle Mass Transfer within Electrostatic Precipitators. *Environ. Sci. Technol.* 40: 3929–3933.

Clack, H.L. (2009). Mercury Capture within Coal-fired Power Plant Electrostatic Precipitators: Model Evaluation. *Environ. Sci. Technol.* 43: 1460–1466.

Clack, H.L. (2012). Estimates of Increased Black Carbon Emissions from Electrostatic Precipitators during Powdered Activated Carbon Injection for Mercury Emissions Control. *Environ. Sci. Technol.* 46: 7327–7333

Clack, H.L. (2013). Computational Modeling of Electrohydrodynamically-Influenced Mercury Adsorption within ESPs. 11th International Conference on Electrostatic Precipitation. Bangalore, India.

Clack, H.L., Gorecki, J., Macherzynski, M., Golas, J., Sherman, L.S. and Blum, J.D. (2013). Interpreting Mercury Capture within a Utility Electrostatic Precipitator through Analyses of Hopper-Segregated Fly Ash Samples 11th International Conference on Mercury as a Global Pollutant. Edinburgh, Scotland.

Clack, H.L. (2016). Numerical 2-D Simulation of Full-scale Dry Sorbent Injection Performance within a Utility Electrostatic Precipitator. *Aerosol Sci. Technol.* Submitted, under Review.

Friedlander, S.K. (2000). *Smoke, Dust and Haze, Fundamentals of Aerosol Dynamics*, Oxford University Press, Oxford.

Hinds, W.C. (1999). *Aerosol Technology: Properties, Behavior, and Measurement of Airborne Particles*, John Wiley & Sons, New York.

IEEE-DEIS-EHD Technical Committee (2003). Recommended International Standard For Dimensionless Parameters Used in Electrohydrodynamics. *IEEE Trans. Dielectr. Electr. Insul.* 19: 3–6.

Kallio, G.A. and Stock, D.E. (1992). Interaction of Electrostatic and Fluid Dynamic Fields in Wire-plate Electrostatic Precipitators. *J. Fluid Mech.* 240: 133–166.

Pavlish, J., Sondreal, E. and Olson, E. (2003). Status Review of Mercury Control Options for Coal-fired Power Plants. *Fuel Process. Technol.* 82: 89–165.

Prabhu, V., Kim, T., Khakpour, Y., Serre, S. and Clack, H.L. (2012). On the Electrostatic Precipitation of Fly Ash-Powdered Mercury Sorbent Mixtures. *Fuel Process. Technol.* 93: 8–12.

Zhao, L. and Adamiak, K. (2008). Numerical Simulation of the Electrohydrodynamic Flow in a Single Wire-Plate Electrostatic Precipitator. *IEEE Trans. Ind. Appl.* 44: 683–691.

Received for review, May 8, 2015
Revised, August 31, 2015
Accepted, September 28, 2015